

Predictions of a Film Coolant Jet in Crossflow With Different Turbulence Models

Asif Hoda

Sumanta Acharya

Mechanical Engineering Department,
Louisiana State University,
Baton Rouge, LA 70803

This study investigates the performance of several existing turbulence models for the prediction of film coolant jet in a crossflow. Two-equation models employing $k-\varepsilon$ and $k-\omega$ closures, broadly categorized as high-Reynolds-number formulations, low-Reynolds-number formulations, DNS-based formulation, and nonlinear formulations have been used to simulate the flow. In all, seven different turbulence models have been tested. Predictions with different models have been compared with experimental results of Ajersch et al. (1995) and with each other to critically evaluate model performance. The assessment of models has been done keeping in mind that all models have been formulated for wall-bounded flows and may not be well suited for the jet-in-a-crossflow situation. Close agreement with experimental results was obtained at the jet exit and far downstream of the jet injection region, but all models typically overpredicted the magnitude of the velocities in the wake region behind the jet. The present study clearly underscores the deficiencies of the current models, and demonstrates the need for improvements. [S0889-504X(00)03002-6]

Introduction

Film cooling of turbine blades is commonly employed to provide effective blade cooling that is needed to ensure long life of the turbine blades and to permit higher turbine inlet temperatures. The interaction of the coolant jet with the crossflow produces a highly complex, three-dimensional flow field in the vicinity of the jet injection. The flow is characterized by both large-scale coherent structures and small-scale turbulence, and the mixing process is controlled by the dynamics of these structures. The coherent structures of primary importance have been identified in the published literature to be jet shear-layer vortices, which dominate the initial portion of the jet, horseshoe vortices, which wrap around the base of the jet, counter-rotating vortex pair (CRVP), which results from the impulse of the jet on the crossflow, and wake vortices formed in the wake of the jet. Accurate prediction of such structures are necessary to correctly predict the jet penetration and reattachment length that are important for heat transfer calculations and the optimization of film cooling effectiveness.

Several experimental studies [e.g., [1–3]] and numerical investigations [e.g., [4–6]] of a jet-in-crossflow have been reported. In the numerical studies, the primary approach adopted has been to use the Reynolds-averaged Navier–Stokes (RANS) solver, which requires the prescription of a turbulence model. The two-equation turbulence models ($k-\varepsilon$ and $k-\omega$) have been used most extensively to simulate a jet-in-crossflow with varying degrees of success. A systematic study of film cooling by Demuren et al. [7] revealed that the very complex flow field established behind the jet was not properly resolved and the turbulent mixing process was crudely simulated with the eddy viscosity model. Demuren [8] also carried out computations using a multigrid method and a second-moment closure model to approximate the Reynolds stresses. Although a fairly good prediction of mean flow trends was reported, there was considerable uncertainty regarding the accuracy of jet penetration height. Multigrid calculations by Claus and Vanka [9] failed to predict the horseshoe vortex even with a highly refined grid. This was attributed partly to the inability of the $k-\varepsilon$ model to resolve the complex turbulence field. Findlay

et al. [10] included the plenum in the computational domain for streamwise inclined jets. The computations underpredicted the streamwise injection of fluid from the jet and the flow field was not in good agreement with experimental results for most of the domain. Ajersch et al. [11] conducted an extensive experimental investigation and a companion numerical simulation using a low-Re $k-\varepsilon$ model along with a nonisotropic extension to the effective viscosity for near-wall turbulence. The streamwise velocity in the jet wake was overpredicted and the recirculation region behind the jet was found to be smaller and closer to the surface than that observed in the measurements. Noticeable overprediction of shear stresses was observed and the simulation could not capture the local minimum in kinetic energy, which was measured in the wake region of the jet.

The varied and often conflicting investigations carried out so far motivate the present study, where several existing turbulence models and their performance in predicting the film cooling flow behavior are evaluated. The focus of this paper is on the fluid dynamic behavior of the jet, and the ability of the turbulence models to reproduce the expected physical behavior correctly. Therefore, heat transfer predictions are not included in the present paper.

Problem Description

The film cooling configuration chosen corresponds to the experimental study of Ajersch et al. [11] where measurements are presented for normal injection through square holes. The physical domain in Fig. 1 shows a single row of six square jets on a flat plate, which represents the turbine blade surface. The computational domain is chosen to be a periodic module and is shown in Fig. 2 and by the dotted lines in Fig. 1. The experimental investigation for this configuration was carried out for velocity ratios $R=0.5$, 1.0, and 1.5. However, the computations have only been carried out for the lowest velocity ratio of $R=0.5$, and the general flow characteristics for this case as predicted by the several models are evaluated by comparison with the measurements.

For the turbulence model to be viable, the main features of the flow are expected to be predicted correctly. In this paper, we evaluate the performance of the models not only by the quantitative comparisons with the measurements reported by Ajersch et al. at a few selected locations (that do not provide a complete

Contributed by the International Gas Turbine Institute and presented at the 44th International Gas Turbine and Aeroengine Congress and Exhibition, Indianapolis, Indiana, June 7–10, 1999. Manuscript received by the International Gas Turbine Institute February 1999. Paper No. 99-GT-124. Review Chair: D. C. Wisler.

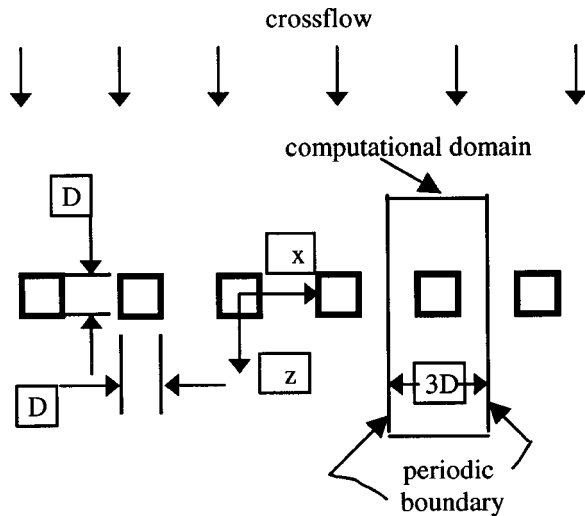


Fig. 1 Schematic of the physical problem

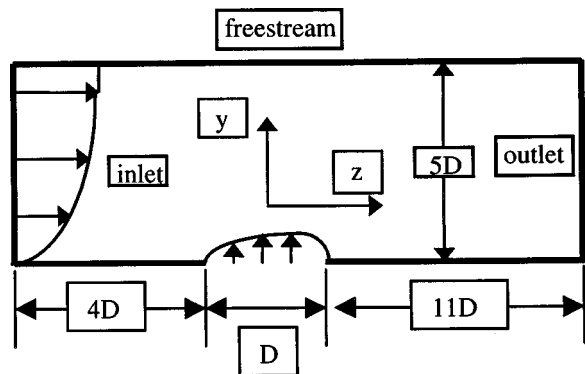


Fig. 2 Side view of the computational domain

description of all the flow features), but also by examining whether the models accurately predict the dominant features of the flow field.

Governing Equations

The steady-state Reynolds-averaged Navier–Stokes equation contains the Reynolds stress tensor $-\rho u'_i u'_j$, which needs to be modeled by a closure approximation. The accuracy of the prediction is based on the adequacy of the closure expressions in capturing the flow physics. The different closure approximations described below include the high-Re models where the near-wall sublayer effects are not resolved, various forms of the low-Re models where the near-wall damping effects are represented by different empirical expressions, and the nonlinear models where turbulence anisotropy is incorporated through nonlinear corrections to the linear stress–strain relations assumed in the linear turbulence models.

Turbulence Models

A number of different models based on the $k-\varepsilon$ and $k-\omega$ closures were used in this study. The various models, under appropriate categories, are listed below:

1 High-Re $k-\varepsilon$ Model. In the standard $k-\varepsilon$ model [12] the Reynolds stress is modeled as

$$-\rho \overline{u'_i u'_j} = -\frac{2}{3} \rho k \delta_{ij} + 2 \mu_t \bar{S}_{ij} \quad (1)$$

The eddy viscosity μ_t is related to the turbulent kinetic energy k and to its dissipation rate ε as

$$\mu_t = \rho C_\mu \frac{k^2}{\varepsilon} \quad (2)$$

Note that Eq. (1) represents a linear relationship between the turbulent stress and the rate of strain, and forms the basis for all linear two-equation models.

The distributions of k and ε in the flow field is determined from their modeled transport equations [12]. The source terms in the modeled equations are given by:

$$S_k = P - \varepsilon; \quad S_\varepsilon = C_{\varepsilon 1} (\varepsilon/k) P - C_{\varepsilon 2} (\varepsilon^2/k) \quad (3)$$

where P is the production of turbulence ($= -\rho \overline{u'_i u'_j} (\partial \bar{U}_i / \partial x_j)$). The high-Re model avoids the need to integrate the modeled equations right down to the wall by making use of the universal behavior of near-wall flows. The standard wall-function approach is thus used to specify the wall boundary conditions for velocity. This is done either in the form of a wall shear stress expression from Couette flow analysis or alternatively by determining the diffusion coefficient on the wall such that the computed shear stress on the wall matches that obtained from the Couette flow analysis.

For the turbulence kinetic energy, a zero value is specified at the wall, while the value of dissipation at a near-wall point is set, using a local equilibrium assumption, as $\varepsilon = C_\mu^{3/4} k^{3/2} / (0.4 \delta y)$.

2 Low-Re Models. The low-Re models resolve the viscous sublayer adjacent to the solid walls and use damping functions that ensure the transition from turbulent stresses to viscous stresses near the wall. The low-Re versions of both $k-\varepsilon$ and $k-\omega$ closure models have been used in this study.

(a) *Low-Re $k-\varepsilon$ Models.* The source terms for k and ε in for the low-Re model take the form:

$$S_k = P - \varepsilon; \quad S_\varepsilon = C_{\varepsilon 1} f_1 \frac{\tilde{\varepsilon}}{k} P - C_{\varepsilon 2} f_2 \frac{\tilde{\varepsilon}^2}{k} + E \quad (4)$$

where

$$\tilde{\varepsilon} = \varepsilon - D \quad \text{and} \quad \mu_t = C_\mu f_\mu \frac{k^2}{\tilde{\varepsilon}} \quad (5)$$

A number of different low Re models [13] have been proposed depending on their use of the functions f_1 , f_2 , and f_μ and the terms D and E . The models used in this study are the Launder–Sharma model [14] and the Lam–Bremhorst model [15]. These two models have been selected due to the asymptotic consistency of their functions in the near wall region as well as in the fully turbulent regime. The Launder–Sharma model uses $\tilde{\varepsilon}$ as the dissipation variable and therefore the term D must asymptote to the nonzero value of ε on the wall and should vanish in the fully turbulent regime where $\tilde{\varepsilon}$ must tend to ε . The term D for the Launder–Sharma model satisfies both the limits, as has been shown by Patel et al. [13]. The asymptotic limits of the damping functions f_2 , f_μ and the term E are also consistent with expectations. The Lam–Bremhorst model, on the other hand, solves for ε itself and therefore the term D is prescribed as zero. The f_μ function for this model shows the correct variation in the near wall region but tends to unity somewhat slowly as compared to the Launder–Sharma model. This model also employs the function f_1 to model the appropriate growth of ε in the region very close to the wall. The f_2 function in this model is modified in order to yield a zero value on the wall. Thus the sink term in the ε equation is damped leading to the expected rapid increase of viscous dissipation as the wall is reached.

(b) *Low-Re $k-\omega$ Model.* The low-Re $k-\varepsilon$ models suffer from the lack of appropriate wall boundary condition for ε , which is specified mostly by ad-hoc empirical functions for the near-wall

flow. The choice of the specific dissipation rate ω is therefore sometimes preferred since the near wall ω behavior is known and therefore the boundary condition at the wall can be specified more accurately. The transport equations for k and ω are given by Wilcox and Traci [16], and have the following source terms:

$$S_k = P - \rho \beta^* \omega k; \quad S_\omega = \alpha \frac{\omega}{k} P - \rho \beta \omega^2 \quad (6)$$

where μ_t is given as $\mu_t = \alpha^* k / \omega$. In implementing this model, all standard functions and constants for the low-Re version of the model, as given by Wilcox and Traci [16], have been used. The functions in this model serve the same purpose as in the low-Re $k-\epsilon$ models and their asymptotic behavior has also been found to be consistent.

3 DNS-Based Low-Re $k-\epsilon$ Model. Rodi and Mansour [17] proposed an improved model for the ϵ equation and a new f_μ function using DNS data for a channel flow. The ϵ -budget computation for the different terms in the ϵ equation was used in conjunction with scaling arguments to obtain the following modeled form of the ϵ equation source term:

$$S_\epsilon = C_{\epsilon 1} \frac{\tilde{\epsilon}}{k} P - C_{\epsilon 2} f_3 f_2 \frac{\tilde{\epsilon}^2}{k} + E \quad (7)$$

The constants and expressions as proposed by Rodi and Mansour [17] have been used here with one exception. The expression for f_3 was given as:

$$f_3 = \exp[2(P/\epsilon)/0.3 \text{Re}_t^{1/2}] \quad (8)$$

The choice of 0.3 in this equation is related to the 0.3 value that the structure function ($= -u'v'/k$) assumes in the center of a channel for fully developed turbulence. Since the flow considered here does not represent a fully developed turbulent channel flow, the factor of 0.3 was found to be inappropriate, and empirical adjustment of this constant led to a value of 2.1.

4 Nonlinear Low-Re Models. Experimental studies carried out for the flow situation being considered here have shown that the flow is highly anisotropic due to strong curvature effects and therefore the nonlinear models listed below have been tested to evaluate their performance in this highly complex flow situation.

(a) *Mayong-Kasagi Model.* Mayong and Kasagi [18] proposed an anisotropic extension to the eddy diffusivity model deduced from the interrelationship among the fundamental processes in the kinetic energy budget. Two additional terms containing quadratic velocity gradients and kinetic energy gradients have been added to the standard linear model. The first of these terms has been derived from the interrelationship between production and dissipation terms in the kinetic energy equation, and plays the role of exhibiting anisotropic characteristics for each Reynolds stress component over the whole flow field except for the immediate vicinity of the wall. The second term added has been derived from the balance between the diffusion and dissipation terms so that the wall-limiting condition for the normal Reynolds stresses is satisfied. The second term, however, does not satisfy the general frame invariance necessary for the broadest range of application, because the invariant condition is not generally satisfied in the immediate vicinity of a plane interface where turbulence is quasi-two-dimensional due to the blocking of a normal velocity component. More details of the model are found in Mayong [19].

(b) *Speziale Model.* Speziale [20] derived a nonlinear model by means of an asymptotic expansion, which satisfies both realizability and invariance requirements. This model is expected to incorporate the streamline curvature effects by introducing quadratic velocity gradient terms and is expected to do better in flows where the differences in normal stresses are significant. Although the use of the original Speziale model has been reported primarily in conjunction with wall functions, it has been implemented here

in a low-Re model form with the damping functions in the near-wall region obtained from the Launder-Sharma model.

Computational Details

The modeled transport equations were solved using a three dimensional CFD code developed by the authors based on the SIMPLE algorithm [21]. A control-volume-based finite difference formulation that uses a second-order accurate central difference scheme for the viscous terms and a power law based scheme for the convective terms has been used. In calculating the source terms in the equations for momentum conservation and turbulence quantities, the first and second-order derivatives were calculated using the Fornberg algorithm [22] employing fourth-order accurate centered differencing scheme for interior points and second-order accurate one-sided differencing for boundary points. A staggered grid arrangement with velocity components stored at the cell faces and all other scalar quantities located at the grid points is employed to avoid checkerboard fields. The system of equations was solved with the Tridiagonal Matrix algorithm employing an underrelaxation procedure to aid convergence.

A nonuniform grid ($59 \times 60 \times 140$) was set up in the computational domain (Fig. 2) with grid points clustered near the bottom wall and around the jet. The jet injection region was resolved with a 19×19 mesh. Inlet profiles for both the crossflow (at $Z/D = -4.5$) and at the exit of the jet hole were provided from the experimental data of Ajersch et al. [11]. The measured data at the crossflow inlet corresponded closely with the $1/7$ th turbulent boundary layer profile with a boundary layer thickness of $2D$. At the jet-hole exit, all three velocity components plus their rms values were available from the measurements, and these were interpolated to prescribe the numerical boundary conditions for both the mean velocity and the turbulence kinetic energy. A periodic boundary condition was implemented in the spanwise direction representing a transverse row of injection holes while at the outlet the normal gradient of all variables was prescribed as zero. At the top plane, free-stream conditions from the measurements were specified.

The equations were nondimensionalized with the mean jet velocity, V_j , and jet width, D , and computations were carried out at a Reynolds number $V_j D / \nu$ of 4700 for a blowing ratio of 0.5. The mass residual in each cell was determined from the continuity equation and the maximum residual was established as the criterion for assessing the overall convergence of the field. At residual levels of 10^{-6} – 10^{-7} , the solution was found not to change and the solution was considered converged in this range. Grid independence was checked by comparing the $59 \times 60 \times 140$ grid (nearly 0.5 million nodes) solution (using the low-Re $k-\epsilon$ Launder-Sharma model) with a more refined $71 \times 90 \times 200$ grid (nearly 1.28 million nodes). The difference in the solution on the two grids was found to be minimal, (maximum difference in the velocity values was less than 3 percent) as shown in Fig. 3.

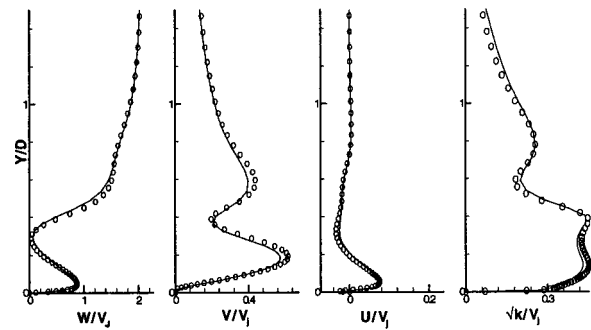


Fig. 3 Grid independence study with the LS model. Velocity and kinetic energy profiles at $X/D=0, Z/D=1$; \bullet $71 \times 90 \times 200$ grid; — $59 \times 60 \times 140$ grid.

Results and Discussion

A discussion of the model predictions and comparisons with the measurements of Ajersch et al. [11] will be presented next. The following nomenclature will be followed hereafter while referring to the various models. The high-Re model will be referred to as HRE, the Launder-Sharma model as LS, the Lam-Bremhorst model as LB, the Mansour-Rodi model as MR, the nonlinear Speziale model as SP, the nonlinear Mayong-Kasagi model as MK, and the $k-\omega$ model as KW.

Mean Velocity and Turbulence Statistics. The mean velocity and turbulence kinetic energy profiles are compared with the experimental results of Ajersch et al. [11] at two spanwise locations: $X/D=0$ along the jet center plane in Fig. 4, and $X/D=-0.5$ along the spanwise edge of the jet in Fig. 5. The figures show how the flow varies with distance Y/D from the wall at various downstream locations ($Z/D=0, 1, 3, 5$ and 8). The main flow features, namely the wake of the jet, the counter-rotating vortex pair (CRVP), and the horseshoe vortex are expected to be clearly evident along the $X/D=0$ and 0.5 streamwise planes, and therefore comparison of model predictions with experimental data along these representative planes is likely to reveal how well the models capture the features of the flow. The flow features are also captured in the plots shown in Fig. 7, which present streamwise vorticity component superimposed by velocity vectors along a cross-stream plane.

Figure 4(a) shows the downstream development of the mean streamwise velocity (W/V_j) along the jet center plane ($X/D=0$). At the jet center ($Z/D=0$), where the jet exit plane boundary condition are specified from experimental data, the model predictions compare well with measurements. One hole-diameter downstream of the jet ($Z/D=1$), a reverse flow region close to the wall is observed in the measurements, which is captured well by the HRE model, but all other models predict a much smaller reverse flow region. The differences in the length of the recirculation regions predicted by the various low-Re models and the HRE model is brought out very clearly by the vector plots presented later in Fig. 9. The HRE model behavior very close to the wall is strikingly different from the other models, which typically show three distinct flow regions at this location: a wall-jet-like layer next to the wall with accelerating flow, a wake region above it where low velocities are observed, and a shear layer with strong velocity gradients due to the velocity changing from low values at the top of the wake region to the free-stream value over a very short vertical distance. The wall-jet layer very close to the wall could not be validated as measurements very close to the wall were not available in the data set used in this study. However, several experimental investigations [23] have revealed that a wall-jet structure does exist close to the wall even for low velocity ratio R , although this effect is stronger for the high R cases. At this location ($Z/D=1$), immediately downstream of the jet, the low pressure in the wake of the jet induces laterally inward motion of the surrounding crossflow fluid close to the wall toward the jet center plane. The entrained fluid moves upward, in the vicinity of the jet center plane, toward the jet and it is then swept up by the bent-over jet (Fig. 9). The inward motion of the high momentum fluid toward the jet center plane close to the wall is partly re-oriented in the streamwise direction and leads to the formation of the wall-jet-like structure (seen in Fig. 7).

Evidence of the wall-jet can also be seen from measurements at $Z/D=3$ where there is a peak close to the wall and the velocities then drop to lower values in the wake region. The steep velocity gradient observed close to $Y/D=1$ represents the shear layer where the velocity changes from low values in the wake of the jet to the free-stream value. All models follow the experimental trends appropriately but typically overpredict the streamwise velocity in the wake region. Also the shear layer is closer to the wall which indicates that the wake-height is underpredicted at this center-plane location.

The large deviations of model predictions observed in the vicinity of the jet (Z/D between 1 and 3) indicate that the near field of the jet, influenced significantly by the dynamical behavior of the large-scale structures, is not properly modeled. The effect produced by the damping functions in the low-Re models is therefore not accurate in the immediate vicinity of the jet.

At farther downstream locations, measurements show that the velocity gradients in the wall-jet layer and the shear layer are diminished, and flow recovery toward a boundary layer profile is observed. The velocity gradients are overpredicted in the wall-jet layer at $Z/D=5$ while agreement with experimental results is better at $Z/D=8$. For Z/D greater than 3, the LB model shows the best agreement with experimental data. The LB model is known to give the correct asymptotic behavior $-w'v' \propto y^4$ in the near-wall region due to the appropriate variation of the f_μ functions in the immediate vicinity of the wall. The f_μ function behavior of the LS model has been found to be more consistent in the fully turbulent regime and therefore it does not do as well as the LB model in the near-wall region. The nonlinear SP model does not show any significant improvements in the mean velocity field predictions and its trends are only slightly different from the LS model. This may in part be due to the fact that in the near-wall region both these models employ the same damping functions and also that the nonlinear quadratic terms introduced in the Reynolds stress terms in the SP model do not make any significant contribution. The MK model, at $Z/D=5$ and $Z/D=8$, underpredicts the streamwise velocity gradients in the shear layer and consequently predicts a deeper penetration of the jet into the crossflow. The performance of the nonlinear models cannot however be judged merely on the basis of mean velocity trends and a proper evaluation of the Reynolds stresses will be carried out in a later section in order to get the correct picture on these nonlinear variants of the $k-\varepsilon$ model.

The secondary motions in the cross-stream plane are evaluated by comparing the vertical velocity profiles in Fig. 4(b) and the cross-stream velocity in Fig. 4(c). The vertical velocity distribution at the jet center ($Z/D=0$) once again shows good agreement with experimental data owing to the measured jet inlet conditions specified at the jet-exit plane. The large vertical velocity values (V/V_j greater than 1) are because the crossflow acts as a partial cover over the jet, causing the jet to bend before leaving the jet exit, and leads to the acceleration of the jet toward the downstream edge of the exit hole. In the reverse flow region, at $Z/D=1$, two peaks are recorded, the first peak off the wall is in the wake region where the reversing fluid is lifted up by the deflected jet, while the second peak corresponds to the deflection of the cross stream over the jet. This trend is closely followed by the models, although the peak values are predicted closer to the wall. This is primarily due to the predicted wake region being much closer to the wall and the jet penetration being underpredicted by the models in the jet center plane. Additionally, the models differ in their prediction of the first peak value off the wall while the second peak is the same for all the low-Re models. The LB model predicts the lowest peak value while the MK model records the highest first peak value with the other models lying in between. These differences are related to the behavior of the damping functions for the various models with the LB model functions being asymptotically consistent while the f_μ function of MK model tends to unity somewhat slowly. The dependence on these functions is further emphasized by the observation that the second peak is the same for all the low-Re models since the functions tend to unity at larger distances from the wall.

Further downstream, at $Z/D=3$, measurements suggest that, as for the streamwise velocity, the wake region is not properly predicted with the predictions showing a faster recovery. Measurements between $Z/D=3$ and 8 show a negative velocity at the top of the bent-over jet, which indicates that the crossflow is coming down at this point. The downwash of the crossflow as well as the low-velocity magnitudes in the wake region are not captured by

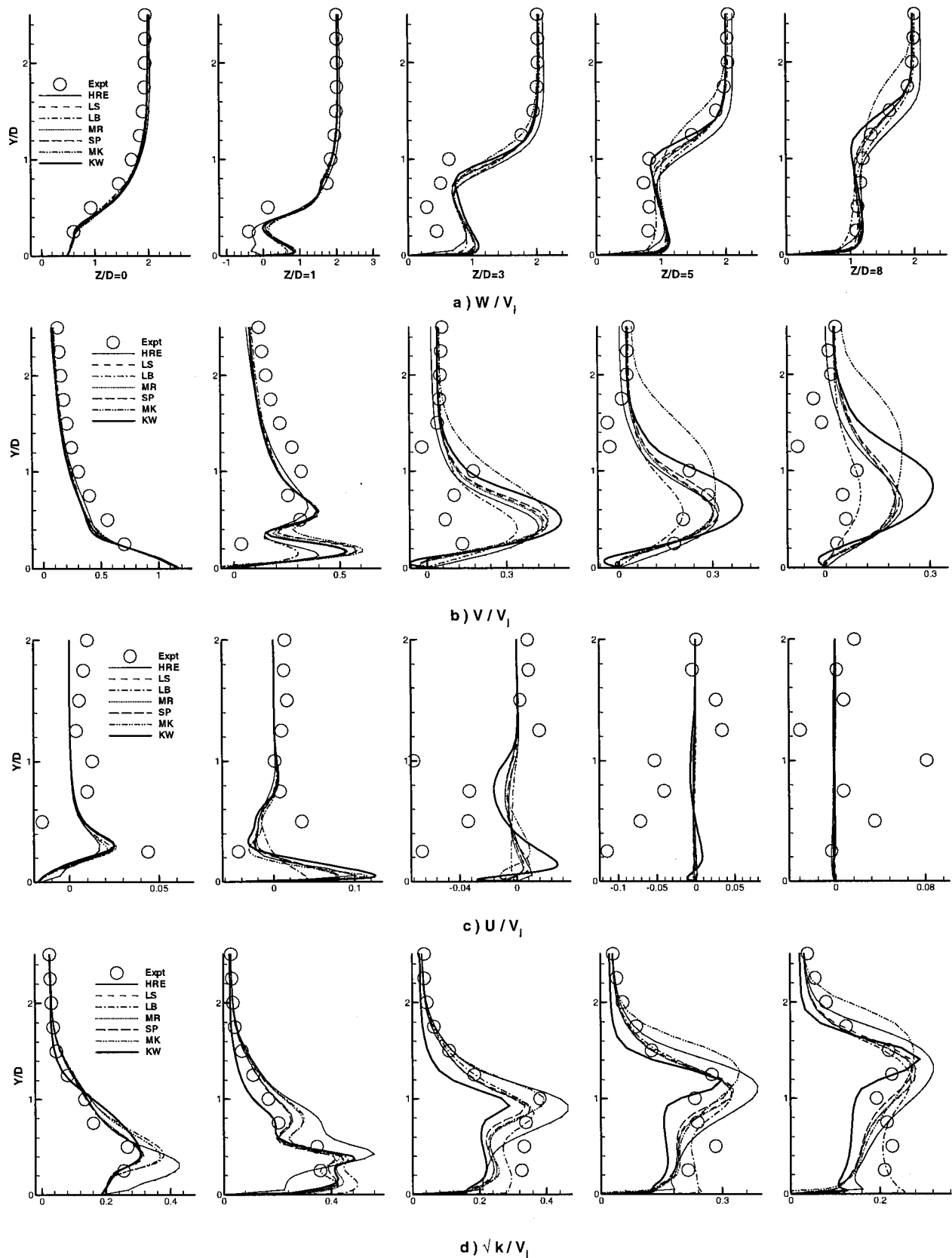


Fig. 4 Velocity and kinetic energy profiles at $X/D=0$ at different Z/D from center of jet

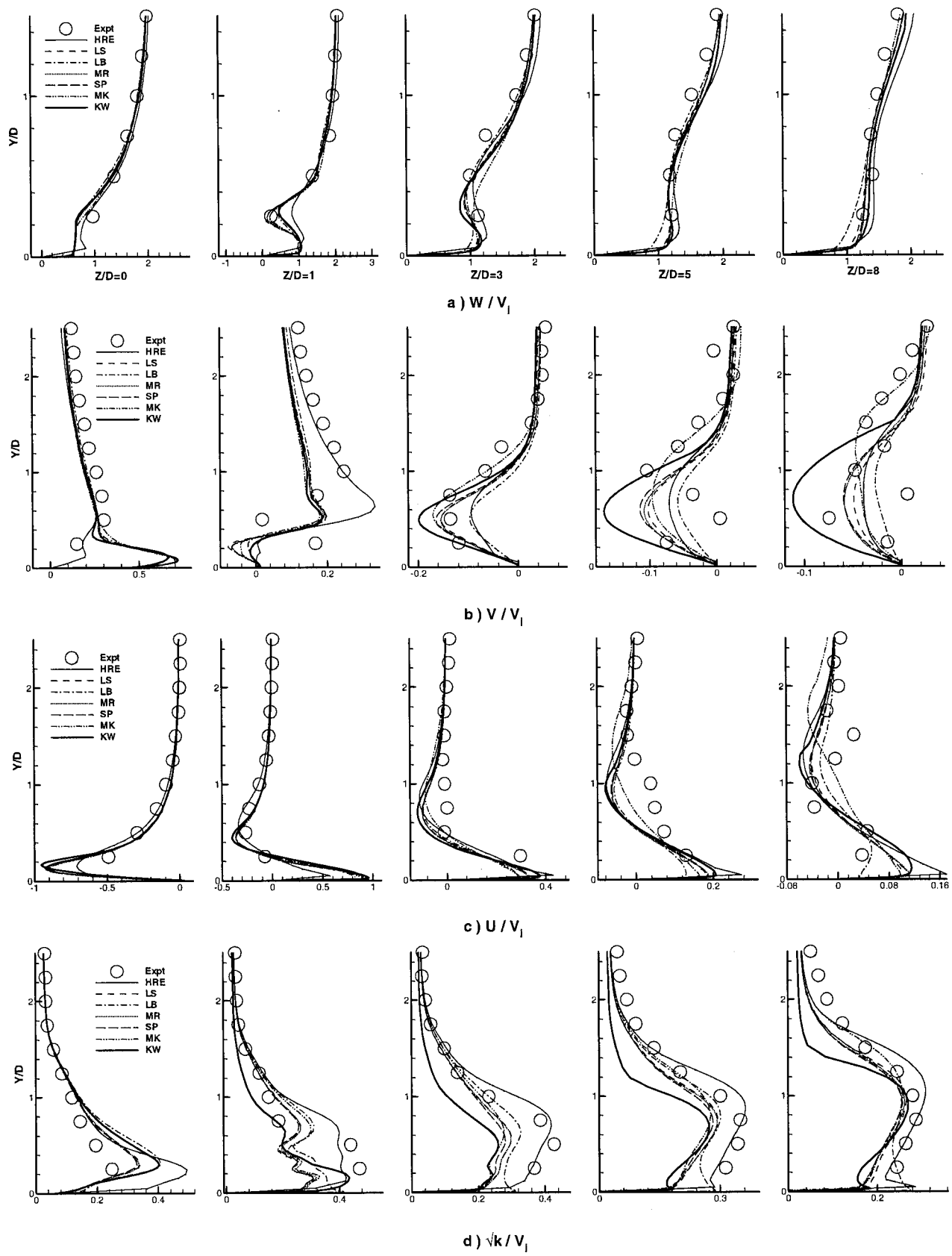


Fig. 5 Velocity and kinetic energy profiles at $X/D = -0.5$ at different Z/D from center of jet

the model predictions. This is probably due to the models' predicting a smaller reverse flow region behind the jet, which implies that the wake effect is not as strong as experimentally observed. The measurements continue to show a dual-peak structure at $Z/D=3$, while the predictions only show a single peak due to the faster flow recovery. The predicted magnitudes at $Z/D=3, 5$, and 8 show the same trends as at $Z/D=1$, with the KW model showing the largest peak values and the LB model showing the smallest magnitudes and the best agreement with the data. The behavior of the MK model at $Z/D=5$ and $Z/D=8$, with the peak shifted upward, is a consequence of the jet penetration being overpredicted at these locations.

The spanwise velocity (U/V_j) presented in Fig. 4(c) should be zero along the jet center plane if the flow at all the inflow planes is symmetric. However, measurements indicate that the inflow at the jet exit plane ($Y/D=0$) is not symmetric with the flow slightly skewed in the lateral direction. This asymmetry in the inlet profile is convected downstream, and is confirmed by the velocity measurements as well as the predictions at the jet exit ($Z/D=0$) and immediately downstream of the jet ($Z/D=1$). As the flow develops downstream, this asymmetry should decrease and the spanwise velocity across the jet-center-plane should become very small. The flow predictions show this trend. However, the measurements show high degree of scatter at downstream locations ($Z/D=5, 8$) and therefore cannot be relied upon.

The kinetic energy (KE) profiles along the jet centerline are shown in Fig. 4(d). The KE distribution is governed by a number of factors, the important ones being the interaction of the oncoming boundary layer and the jet, production due to the various velocity gradients $\partial W/\partial Y, \partial V/\partial Z, \partial U/\partial X$ and strong streamline curvature effects especially in the vicinity of the jet. At the jet center plane however, the production due to the gradient $\partial W/\partial X$ seems to be the dominant process as a close correlation between the velocity gradient $\partial W/\partial Y$ (Fig. 4(a)) and the KE (Fig. 4(d)) can be seen. The peak KE values occur at approximately the same locations as the peak velocity gradient positions. The HRE, LB, and MK models overpredict the peak values at the jet center ($Z/D=0$) while the other models show close agreement with measurements. The experimental profile at $Z/D=1$ shows peak values in the wall-jet and lower-wake regions and in the shear layer where strong gradients $\partial W/\partial Y$ occur. Model predictions show three peak values corresponding to the strong gradients in the wall-jet layer, the lower-wake region, and the shear layer. The HRE model overpredicts peak values in the wake region and in the shear layer. Farther downstream at $Z/D=3$ and $Z/D=5$ two distinct peaks are observed in the measurements, which once again correspond to the strong velocity gradient $\partial W/\partial Y$ at these positions. The nonlinear and the low-Re $k-\varepsilon$ model predictions in the shear layer are in good agreement with measurements at $Z/D=3$, but the HRE model overpredicts the peak level in this region while the KW model underpredicts the turbulence peak. The models do not behave appropriately in the wake region and are unable to capture the peak value accurately in the wake at $Z/D=3, 5$ and $Z/D=8$. The LB model once again gives better predictions at these locations. However, the KW model significantly underpredicts the KE levels in the wake region. The behavior of the models in the near-wall region is influenced by the dissipation rate ε , which forms the sink term in the KE equation. The ε level in the near-wall region is controlled by the functions f_1, f_2 and the term E . Both f_1 and E tend to increase the value of ε near the wall and thereby reduce the KE levels. The influence of f_1 is confined to a region very close to the wall in case of the LB model, while it is unity for the other models. The term E is therefore dominant in the growth of ε near the wall. The LB model has E equal to zero as the model solves for the dissipation rate itself and therefore the KE level in the near wall region is higher as compared to the other models. Clearly, it is more attractive to solve for ε from a physical point of view. The KW model greatly underpredicts the KE levels in the wake region. As in the case of

the low-Re $k-\varepsilon$ models, the function α multiplying the production term in the ω equation along with the constant β , which tends to decrease the destruction term, lead to very high values of ω in the near-wall region. The combined effect is to reduce the KE levels near the wall. The KE trends in the KW model case suggest that the model functions in the ω equations are not appropriate as they lead to drastic reduction of the kinetic energy. The nonlinear models do not show any significant improvements over their linear counterparts and are unable to predict the correct magnitudes in the wake.

The profiles along the edge of the jet ($X/D = -0.5$) are shown in Fig. 5. The streamwise velocity at different downstream locations is expectedly higher than that along the jet center line (Fig. 4(a)), due to the weaker wake effect, which also results in reduced velocity gradients $\partial W/\partial Y$. The wall-jet layer is also noticed here at $Z/D=1$ with steep gradients in this region and in the shear layer region above the wake. The wake can be seen distinctly at this location, and all the models appear to capture the wake region well except the high-Re model. The wake gradually diminishes with increasing downstream distances, and beyond $Z/D=3$ close agreement with experimental data is shown by all the models.

Vertical velocity comparisons have been shown in Fig. 5(b). As at $Z/D=0$ (Fig. 4(a)), velocities as high as 0.8 times the free-stream velocity are predicted over the jet inlet hole due to the partial cover effect of the crossflow causing the flow to accelerate toward the downstream end. The measurements however do not show this peak at $Z/D=1$, and instead show two peak values; the one closer to the wall is due to the upward motion caused by the CRVP while the other peak at a larger distance from the wall is once again due to the crossflow deflected over the bent-over jet. The predictions show large near-wall deviations from the measured values with negative values close to the wall turning positive around $Y/D=0.3$. The negative values close to the wall represent the outer downward moving parts of the CRVP, while the positive values represent the upper portions of the CRVP and the crossflow regions deflected upward by the jet. Since the measurements do not show negative values close to the wall, it may be concluded that the CRVP in the experiments has a smaller lateral spread relative to the predictions. At Z/D locations farther downstream, the measured and predicted velocities are primarily negative representing the downwash side of the CRVP. The measured behavior is captured well by the models at $Z/D=3$ where the KW model overpredicts the peak downward velocity while the LB model underpredicts it. The experimental measurements shows some scatter in the data at $Z/D=5$ and $Z/D=8$ locations, although the general trend of the jet and the crossflow velocities are downward toward the wall. The downward trend is maintained by the model predictions, but no meaningful comparison can be made with the experimental measurements due to the scatter in the data. In comparing the model predictions with each other, they follow the same trends as observed along the jet center line in Fig. 4 and therefore the arguments extended earlier to account for the model predictions are valid here as well.

Spanwise velocity comparisons in Fig. 5(c) indicate that the model predictions show good agreement with experimental profiles. The spanwise velocities are quite significant at the edge of the jet, and U/V_j reaches values as high as 1 close to the wall. At $Z/D=0$ the spanwise velocity near the lower surface is negative, which indicates that the flow is outward and away from the jet center plane. Close agreement with measurements is observed at this location where the HRE model shows a relatively lower peak value. At $Z/D=1$, the velocities are all positive close to the wall, indicating flow toward the jet centerline. The CRVP entrains the surrounding crossflow fluid close to the wall resulting in positive cross-stream velocity near the wall. The velocity changes sign further away from the wall representing the upper half of the CRVP where the flow is moving away from the centerline. The peak negative value is obtained in the top regions of the CRVP structure and the models are in good agreement with measure-

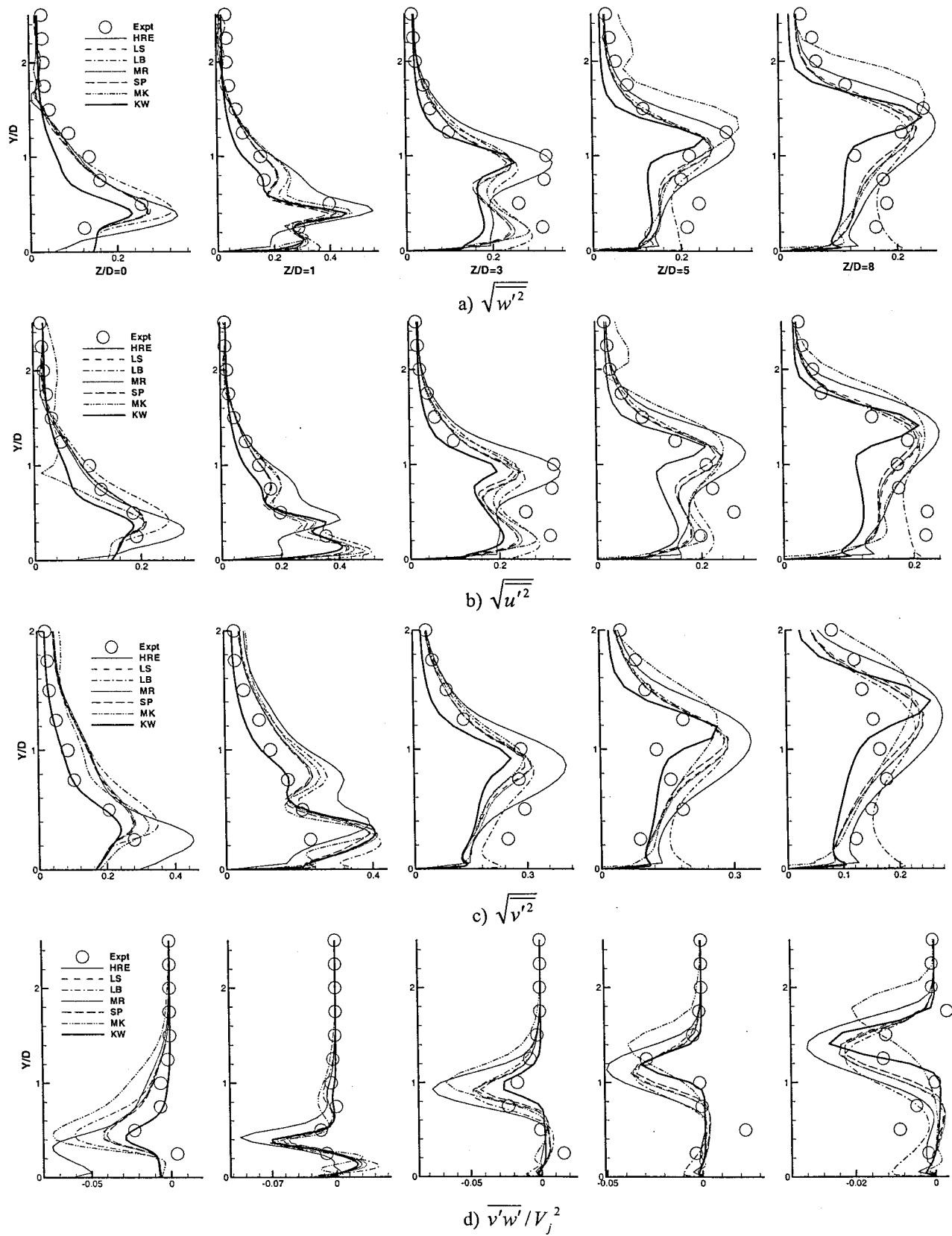


Fig. 6 Stress profiles at $X/D=0$ at different Z/D from center of jet

ments here. As the flow progresses downstream, the CRVP structure diminishes in strength as seen from the experimental profile at $Z/D=3$. Models on the other hand predict a stronger structure at this location. At $Z/D=5$, both the measurements and predictions show a reduction in the strength of the CRVP. However, the measurements do not show any negative values along the top half, indicating a pinched CRVP structure with a wider base and a narrower neck. Predictions, on the other hand, show negative velocities on the top half of the CRVP, both at $Z/D=5$ and 8, indicating a CRVP that is more dispersed in the lateral direction than the experiments. The CRVP cannot be distinctly identified in the measurements at $Z/D=8$ where the scatter in the data indicates that the structure has diminished in strength considerably. The models on the other hand show a distinct structure at this location. The LB model gives better predictions, as before, in the near-wall region at $Z/D=5$ and $Z/D=8$.

Kinetic energy profiles along the edge of the jet correspond to those in a developing boundary layer except in the immediate vicinity of the jet at $Z/D=0$ and $Z/D=1$. At $Z/D=0$ the models follow the experimental trends closely, but overpredict the peak level. Once again, a close correspondence between the velocity gradient $\partial W/\partial Y$ and KE trends is observed at $Z/D=1$ where the peak values correspond to the maximum gradient locations. At this location however, the contribution of the gradient $\partial U/\partial X$ has been found to be significant, largely due to the strong entrainment of the crossflow into the wake region. Model predictions typically show a number of local peak values corresponding to the large spanwise velocity gradients. At downstream locations the experimental profiles are like those in a boundary layer and the models mimic this behavior appropriately, but they underpredict the peak KE levels. The LB and KW models show peak values very close to the wall at $Z/D=5$ and $Z/D=8$, and this is once again related to the steep stream-wise velocity gradients in the near wall region observed at these locations.

The normal stress profiles along the jet center plane ($X/D=0$) are presented in Fig. 6. The experimental w'^2 profiles in Fig. 6(a) shows a correlation to the KE profile and the streamwise normal velocity gradient $\partial W/\partial Y$ in Fig. 5(d). This correlation is particularly strong in the far field ($Z/D>5$) where peak values are obtained in the jet shear-layer region associated with high $\partial W/\partial Y$ and turbulence production. In the near field, peak w'^2 values are observed in the shear layer and in the wall-jet region where large $\partial W/\partial Y$ gradients are found. The correlation between w'^2 and $\partial W/\partial Y$ is not taken into account by the linear eddy viscosity models where the stress w'^2 is assumed to be directly proportional to the gradient $\partial W/\partial Z$ and therefore any simple eddy viscosity model is not expected to do well in this highly complex flow situation.

The measured trends of the stress u'^2 in Fig. 6(b) also show correlation with $\partial W/\partial Y$. In the near field ($Z/D=1$), however, the near-wall behavior also appears to correlate well with $\partial U/\partial X$, which is high close to the surface due to the entrainment of the crossflow boundary layer into the wake region. The anisotropy in the near field of the jet injection close to the wall is clearly evident, and is associated with the dominance of the coherent structures in these regions. However, the low-Re and nonlinear models are found to reproduce this nonisotropic effect in a qualitatively satisfactory manner. At further downstream locations the dependence on the gradient $\partial W/\partial Y$ becomes stronger, especially in the wake of the jet, where the normal stresses w'^2 and u'^2 show trends similar to the KE profiles. Models underpredict the stress levels in the wake region for $Z/D\geq 3$ where the LB model gives better predictions in the near wall region. The anisotropy of the flow in the vicinity of the jet is further demonstrated by the v'^2 profiles at $Z/D=0$ and $Z/D=1$ in Fig. 6(c). In the near field, the v'^2 profiles appear to scale with $\partial V/\partial Y$. At $Z/D=3$ and $Z/D=5$, however, the effect of the gradient $\partial W/\partial Y$ is apparent here

with the peak v'^2 value occurring in the shear-layer region. The profile flattens out as the flow moves farther downstream and at $Z/D=8$ a closer correspondence can be seen with the velocity gradient $\partial W/\partial Y$ rather than with $\partial V/\partial Y$ (see Fig. 4(b)). The normal stresses are therefore not represented appropriately by the models. In the near field, the turbulence exhibits significant anisotropy. The flow field becomes more isotropic farther downstream, but the gradient approximations relating u'_i to $\partial U_i/\partial X_i$ do not appear to be valid. Rather all stresses appear to correlate with $\partial W/\partial Y$.

The profiles for the shear stress $w'v'$ is presented in Fig. 6(d). The peak values observed in the measurements and predictions are in the jet-shear-layer regions and is a consequence of the high $\partial W/\partial Y$ in the shear layer region. This dependence is consistent with the fact that the product $v'^2\partial W/\partial Y$ is the dominant term in the production of $w'v'$. Peak values are overpredicted by the models at $Z/D=0$ location and only the KW model follows the experimental trends closely. The peak values decrease as the flow moves downstream where the streamwise velocity gradients are reduced in the shear layer. At $Z/D=3$ and beyond, the stress values are very small in the wake region, where the velocities are low and fairly uniform. Model predictions in the recirculation region and farther downstream follow the measured trends correctly, largely due to the fact that the eddy viscosity model also incorporates the dependence of $w'v'$ on $\partial W/\partial Y$. The shear stress predicted by the models is found to change sign close to the wall at $Z/D=1$ and is seen to follow the velocity trends reported in Fig. 4(a) where velocity gradients also change sign close to the wall.

In general, the model predictions for the turbulent shear stress $w'v'$ follow the measured trends fairly well in the shear layer and also reflect the appropriate dependence on velocity gradients. In comparing the model predictions, the HRE model shows the greatest level of overprediction in the peak stress levels. This would lead to the greatest levels of turbulent transport, and is consistent with the observation that the HRE model is associated with the highest lateral jet penetration. The failure of the nonlinear models to give better predictions over the linear ones was somewhat unexpected. The introduction of the nonlinear quadratic terms in the stress-strain relationship in order to incorporate the effect of strong streamline curvatures are therefore insufficient and cubic terms must be included in order to obtain the desired stress-strain coupling. The introduction of merely quadratic terms in the SP and MK models do not produce the desired effect of streamline curvatures on the stress levels.

Vector Plots and Vorticity Contours. Attention is now turned toward describing the overall features of the flow field by presenting vorticity contours and vector plots along a typical cross-stream plane. Figure 7 presents the velocity vectors superimposed on the streamwise vorticity contours at $Z/D=3$ cross-stream plane. The predictions for all seven models evaluated are presented, and in each figure the same gray scale is used in order to facilitate a comparison between the different model predictions.

At $Z/D=3$, the CRVP is clearly established and is the dominant feature in the flow field. The HRE model shows the greatest lateral spread, which was also observed in the velocity comparisons shown in Fig. 5, where the spanwise velocities predicted by the HRE model are larger than those predicted by the other models. The MK model shows the greatest vertical spread of the jet, and this was also observed in Fig. 4, where in the MK model predictions, the shear layer region was displaced vertically upward relative to other models and the measurements. The LB model predictions show the weakest CRVP, and the lowest levels of vertical and lateral spread. All the low-Re models show small negative velocities close to the wall between X/D of -1 and -1.5, and these reflect the manifestation of the horseshoe vortex. It is the strongest, and can be clearly observed in the KW model

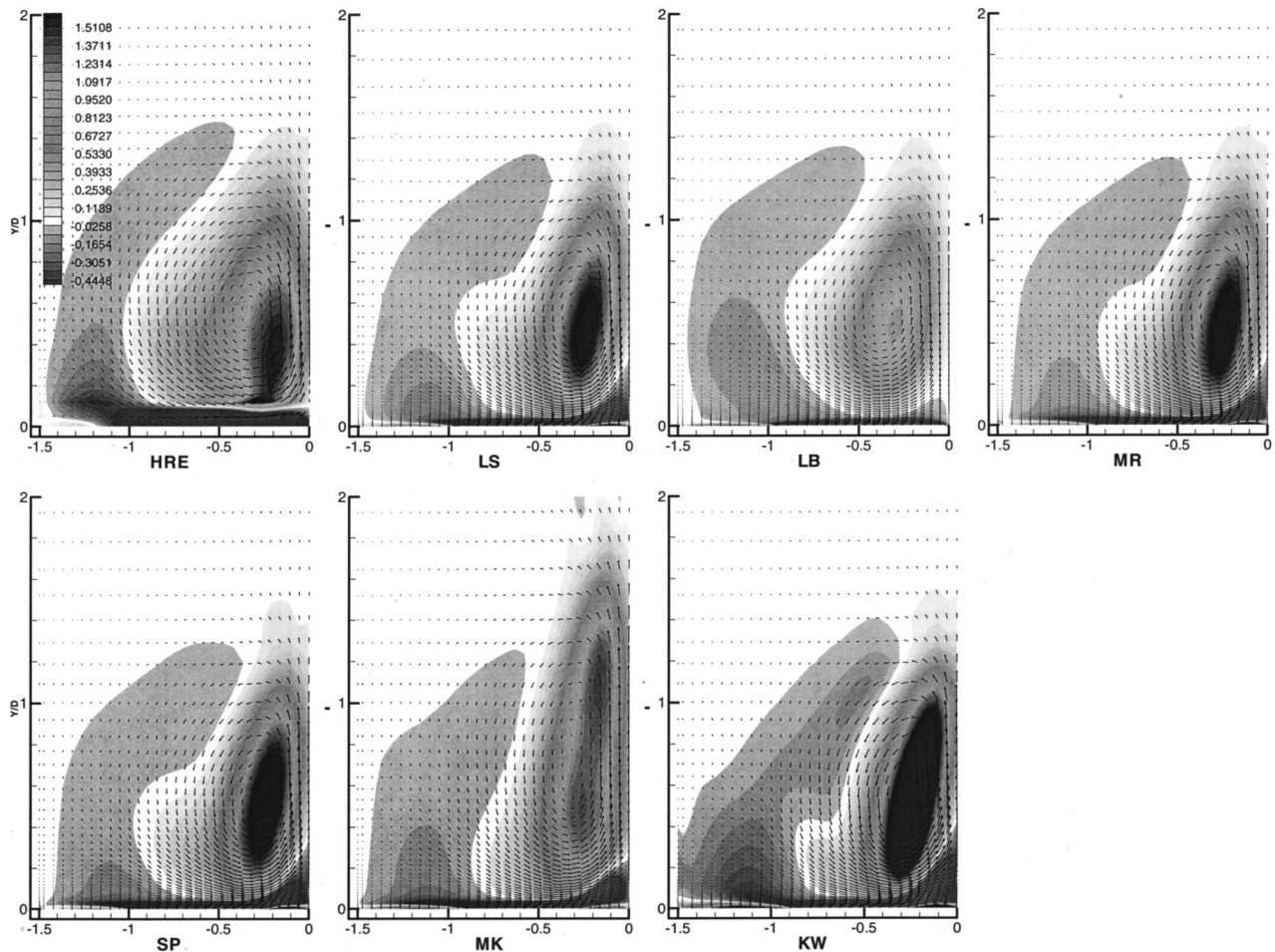


Fig. 7 Z component of vorticity and velocity vectors in X-Y plane at $Z/D=3.0$ for different models

predictions. Also of interest is the clear development of a wall-vortex structure in all the low-Re models. The wall-vortex is a manifestation of the crossflow entrainment into the wake region encountering an adverse pressure gradient in the spanwise direction near the jet centerplane. This adverse pressure gradient leads to flow reversal in the spanwise (XY) plane and the formation of the wall vortex structure close to the surface (as captured by the low-Re models). The vortex is confined between X/D of 0 and -0.5 at this Z/D location. As for the horseshoe, the KW model predicts the strongest wall vortex structure. Note that the HRE model does not predict the wall vortex at all.

Details of the horseshoe vortex predicted at $Z/D=8$ location are shown in an enlarged view in Fig. 8. The horseshoe can be clearly observed in all the model predictions, and show significant differences in size and strength, with the KW model showing the most significant horseshoe structure.

The differences in the recirculation region behind the jet are presented in greater detail in Fig. 9, which shows that the recirculation in all the low-Re models is qualitatively similar, with the reversed flow being entrained upward into the jet and then carried forward along its trajectory. The HRE model shows a much larger region of negative streamwise velocity, with strong crossflow entrainment into the wake. The recirculation region in the HRE model extends all the way to $Z/D=1.5$, while in the other models the recirculation region is less than $1D$ from the center of the jet-exit.

The region upstream of the jet marks the inception of the horseshoe vortex. An exploded view of this region is shown in Fig. 10, where the KW model, the SP model, and the MR model all show the inception of the horseshoe at this $X/D=0$ centerplane. Since all models show the horseshoe vortex at constant- Z/D planes further downstream (see Figs. 7 and 8), this implies that for the

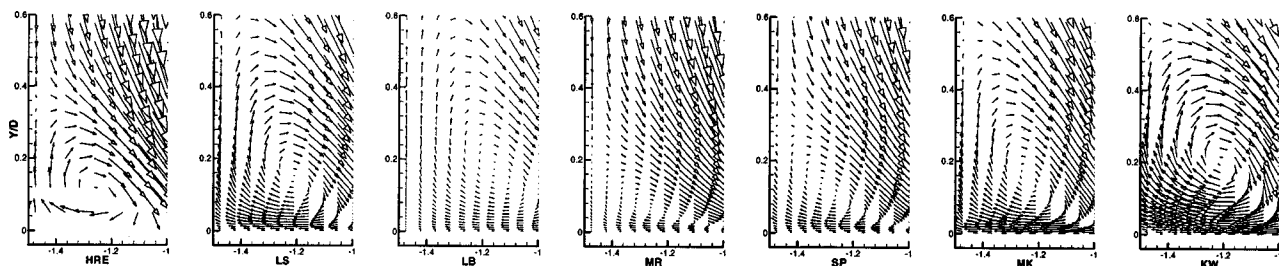


Fig. 8 Velocity vectors in X-Y plane at $Z/D=8$

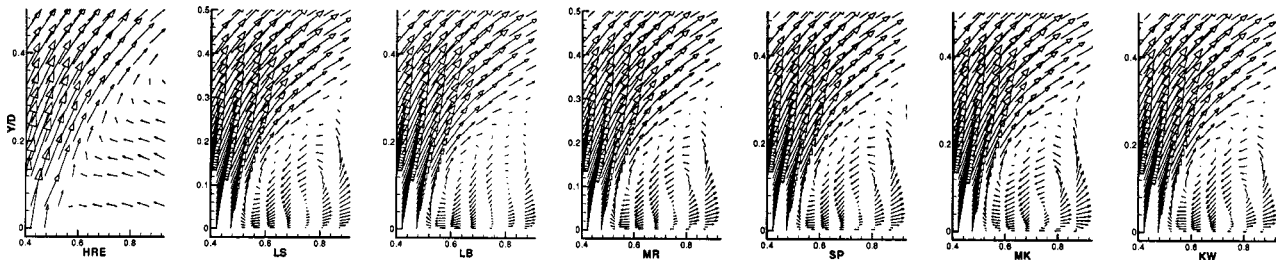


Fig. 9 Velocity vectors in $Y-Z$ plane at $X/D=0$

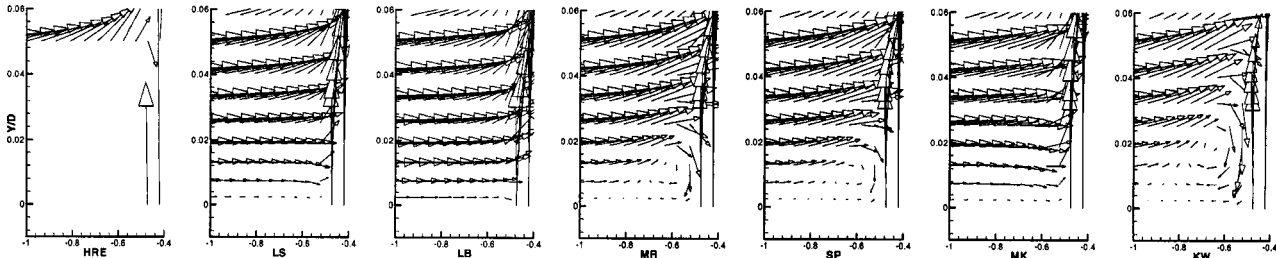


Fig. 10 Velocity vectors in $Y-Z$ plane at $X/D=0$

models where the horseshoe is not observed at $X/D=0$ in Fig. 10, the inception may occur at other X/D planes. Evidence of this is seen in streamwise and spanwise vorticity contours (not shown here) at a constant Y/D plane ($=0.05$) very close to the wall.

Concluding Remarks

Numerical predictions for film cooling jet in a crossflow have been carried out in this study using seven different turbulence models: a high-Re model (HRE), low-Re models (LS, LB, KW), nonlinear models (SP, MK), and a DNS based low-Re model (MR). The mean flow velocity and turbulent statistic profiles in general agree fairly well with experimental trends. The CRVP is distinctly predicted by all the models, but only a few models manage to capture the horseshoe structure correctly for the low blowing ratio case considered in this paper. The HRE model is not very well suited for the specific flow situation as it does not resolve the near-wall region properly. Although the mean flow profiles are predicted well, the turbulence levels are overpredicted and the HRE model is also unable to capture the recirculation in front of the jet. The HRE model predicts the largest levels of spanwise-jet-penetration, and substantially overpredicts the measured values of the spanwise and vertical velocities. The use of this model in such a complex flow situation is therefore not recommended. The LS model, which resolves the near-wall region, follows the experimental trends correctly, but fails to predict the correct trends in the wake of the jet, and does not represent the turbulent mixing taking place in this region appropriately. The near-wall region behavior of the LB model is consistently good, and this model, in general, seems to provide the best agreement with measurements. Compared to the other models, the LB model shows the smallest levels of vertical and spanwise spread. However, predictions in the jet region do not follow the experimental trends correctly, and the model is also unable to capture the recirculation in front of the jet. This structure is distinctly captured by the MR model. In this region the gradients in the vertical direction are of primary importance and the scaling arguments used for deriving the correlation terms in the ε -budget [17] hold good. In the jet and its vicinity, however, the gradients in the other directions cannot be neglected, and therefore the simplified ε budget is inadequate in the jet and its wake region. Clearly, the ε budget needs to be optimized for the present flow situation using DNS

data on lines similar to the MR model. The SP model predicts the turbulent characteristics trends correctly, but like the other models it is unable to resolve the variations observed in the wake of the jet. The MK nonlinear model significantly overpredicts the vertical jet penetration. The inability of the SP and MK nonlinear models to give better predictions compared to the linear models is thought to be a consequence of the fact that the nonlinear model coefficients were obtained through curve fitting of experimental data for simple wall bounded flows [18,20] and may not be well suited for the jet in a crossflow situation. The improved predictions of the near-wall structures obtained with the KW model can be attributed in part to the fact that the boundary conditions specified for ω are more accurate than those for ε . This problem related to the ε behavior near the wall has been pointed out by a number of researchers.

It is therefore clear from the present study that the models in their present form give overly simplistic predictions for the highly complex flow field being considered here. A comparison of the model predictions clearly reveals the need for better resolution of the near-wall region, asymptotic consistency of model coefficients, and damping functions in the jet and wall-bounded regions, respectively, and an appropriate representation of the ε budget. Also required is a suitable nonlinear formulation to predict the nonisotropic nature of the flow accurately. An effort along these directions using DNS predictions for jet in a crossflow [24,25] to guide the model development is being made by the authors and is to be reported shortly.

Acknowledgments

This work was done with support from NASA-Lewis (Grant No. NAG3-1641). Dr. Chi Wang and Dr. Ray Gaugler served as contract monitors. Their support is gratefully acknowledged.

Nomenclature

- $C_\mu, C_{\varepsilon 1}, C_{\varepsilon 2}$ = empirical constants appearing in $k-\varepsilon$ turbulence models
- D = function used in the low-Reynolds-number $k-\varepsilon$ model; also jet diameter (=jet width)
- E = function used in the low-Reynolds-number $k-\varepsilon$ model

f_1, f_2, f_μ	= empirical functions of turbulent Reynolds number in low-Re $k-\varepsilon$ models
f_3	= empirical function used in the Mansour-Rodi $k-\varepsilon$ model
k	= turbulent kinetic energy
P	= turbulence production term
R	= jet-to-crossflow velocity ratio
Re_t	= turbulent Reynolds number
U, V, W	= mean velocity components in x , y , and z directions, respectively
$\frac{V_j}{u'_j}$	= mean jet velocity
$\frac{u'_i u'_j}{u'^2}, \frac{v'^2}{u'^2}, \frac{w'^2}{u'^2}$	= Reynolds stresses
$u'v', v'w', u'w'$	= normal stresses with respect to x, y, z axes
$u'v', v'w', u'w'$	= shear stresses
x	= coordinate in the cross-stream direction
y	= coordinate normal to the wall
z	= coordinate in the streamwise direction
$\alpha, \alpha^*, \beta^*$	= empirical functions in the $k-\omega$ model
β	= empirical constant in the $k-\omega$ model
ε	= rate of dissipation of kinetic energy
$\tilde{\varepsilon}$	= modified dissipation rate
μ, μ_t	= dynamic and turbulent viscosity
ν, ν_t	= kinematic and turbulent kinematic viscosity
ρ	= density
σ	= Prandtl number
ω	= specific dissipation rate = ε/k

References

- [1] Fric, T. F., and Roshko, A., 1994, "Vortical Structures in the Wake of a Transverse Jet," *J. Fluid Mech.*, **279**, pp. 1-47.
- [2] Lee, S. W., Lee, J. S., and Ro, S. T., 1994, "Experimental Study on the Flow Characteristics of Streamwise Inclined Jets in Crossflow on Flat Plate," *ASME J. Turbomach.*, **116**, pp. 97-105.
- [3] Kelso, R. M., Lim, T. T., and Perry, A. E., 1996, "An Experimental Study of Round Jets in Crossflow," *J. Fluid Mech.*, **306**, pp. 111-144.
- [4] Garg, V. K., and Gaugler, R. E., 1997, "Effect of Coolant Temperature and Mass Flow on Film Cooling of Turbine Blade," *Int. J. Heat Mass Transf.*, **40**, No. 2, pp. 435-445.
- [5] Kim, S. W., and Benson, T. J., 1993, "Fluid Flow of a Row of Jets in Crossflow—A Numerical Study," *AIAA J.*, **31**, No. 5, pp. 806-811.
- [6] Walters, D. K., and Leylek, J. H., 2000, "A Detailed Analysis of Film-Cooling Physics: Part I—Streamwise Injection With Cylindrical Holes," *ASME J. Turbomach.*, **122**, pp. 102-112.
- [7] Demuren, D. K., Rodi, W., and Schonung, B., 1986, "Systematic Study of Film Cooling With a Three-Dimensional Calculation Procedure," *ASME J. Turbomach.*, **108**, pp. 124-130.
- [8] Demuren, A. O., 1993, "Characteristics of Three-Dimensional Turbulent Jets in Crossflow," *Int. J. Eng. Sci.*, **31**, No. 6, pp. 899-913.
- [9] Clauss, R. W., and Vanka, S. P., 1990, "Multigrid Calculations of Jet in Crossflow," *AIAA Paper No. 90-0444*.
- [10] Findlay, M. J., He, P., Salcudean, M., and Gartshore, L. S., 1996, "A Row of Streamwise-Inclined Jets in Crossflow: Measurements and Calculations," *ASME Paper No. 96-GT-167*.
- [11] Ajersch, P., Ketler, S., Zhou, J. M., Gartshore, I., and Salcudean, M., 1997, "Multiple Jets in a Crossflow: Detailed Measurements and Numerical Simulations," *ASME J. Turbomach.*, **119**, pp. 330-342.
- [12] Launder, B. E., and Spalding, D. B., 1974, "The Numerical Computation of Turbulent Flows," *Comput. Methods Appl. Mech. Eng.*, **3**, No. 2, pp. 269-289.
- [13] Patel, V. C., Rodi, W., and Scheuerer, G., 1985, "Turbulence Models for Near-Wall and Low-Reynolds Number Flows: A Review," *AIAA J.*, **33**, pp. 1308-1318.
- [14] Launder, B. E., and Sharma, B. I., 1974, "Application of the Energy Dissipation Model of Turbulence to the Calculation of Flow Near a Spinning Disc," *Lett. Heat Mass Transfer*, **1**, pp. 131-138.
- [15] Lam, C. K. G., and Bremhorst, K. A., 1981, "Modified Form of the $k-\varepsilon$ Model for Predicting Wall Turbulence," *ASME J. Fluids Eng.*, **103**, 456-460.
- [16] Wilcox, D. C., and Traci, R. M., 1976, "A Complete Model of Turbulence," *AIAA Paper No. 76-351*.
- [17] Rodi, W., and Mansour, N. N., 1993, "Low Reynolds Number $k-\varepsilon$ Modelling With the Aid of Direct Simulation Data," *J. Fluid Mech.*, **250**, pp. 509-529.
- [18] Mayong, H. K., and Kasagi, N., 1990, "Prediction of Anisotropy of the Near-Wall Turbulence With an Anisotropic Low-Reynolds-Number $k-\varepsilon$ Turbulence Model," *ASME J. Fluids Eng.*, **112**, pp. 521-524.
- [19] Mayong, H. K., 1988, "Fundamental Studies on Two-Equation Turbulence Models for Numerical Prediction of Wall-Bounded Shear Flows and Heat Transfer," Dr. Eng. Thesis, The University of Tokyo.
- [20] Speziale, C. G., 1987, "On Nonlinear $k-l$ and $k-\varepsilon$ Models of Turbulence," *J. Fluid Mech.*, **178**, pp. 459-475.
- [21] Patankar, S. V., 1980, "Generation of Finite Difference Formulas on Arbitrarily Spaced Grids," *Math. Comput.*, **31**, No. 184, pp. 699-706.
- [22] Fornberg, B. G., 1988, "Generation of Finite Difference Formulas on Arbitrarily Spaced Grids," *Math. Comput.*, **31**, No. 184, pp. 699-706.
- [23] Andreopoulos, J., and Rodi, W., 1984, "Experimental Investigation of Jets in a Crossflow," *J. Fluid Mech.*, **138**, pp. 93-127.
- [24] Muldoon, F., and Acharya, S., 1999, "Dynamics of Large-Scale Structures for Jets in a Crossflow," *ASME J. Turbomach.*, **121**, pp. 577-588.
- [25] Sharma, C., and Acharya, S., 1998, "Direct Numerical Simulation of a Coolant Jet in a Periodic Crossflow," *Heat Transfer in Turbomachinery*, ASME HTD-Vol. 361-3/PID-Vol. 3, p. 363.